Monthly Notices of the ROYAL ASTRONOMICAL SOCIETY

MNRAS **491,** 3419–3434 (2020) doi:10.1093/mnras/stz3190
Advance Access publication 2019 November 18

Mass and star formation rate of the host galaxies of compact binary mergers across cosmic time

M. Celeste Artale [1]★ Michela Mapelli,[1,2,3,4] Yann Bouffanais,[2] Nicola Giacobbo [2,3,4] Mario Pasquato[3,4] and Mario Spera [1,2,3,4,5,6]

[1]*Institut für Astro- und Teilchenphysik, Universität Innsbruck, Technikerstrasse 25/8, A-6020 Innsbruck, Austria*
[2]*Physics and Astronomy Department Galileo Galilei, University of Padova, Vicolo dell'Osservatorio 3, I-35122, Padova, Italy*
[3]*INAF – Osservatorio Astronomico di Padova, Vicolo dell'Osservatorio 5, I-35122, Padova, Italy*
[4]*INFN-Padova, Via Marzolo 8, I-35131 Padova, Italy*
[5]*Center for Interdisciplinary Exploration and Research in Astrophysics (CIERA), Evanston, IL 60208, USA*
[6]*Department of Physics and Astronomy, Northwestern University, Evanston, IL 60208, USA*

Accepted 2019 November 8. Received 2019 October 30; in original form 2019 September 17

ABSTRACT

We investigate the properties of the host galaxies of compact binary mergers across cosmic time, by means of population-synthesis simulations combined with galaxy catalogues from the EAGLE suite. We analyse the merger rate per galaxy of binary neutron stars (BNSs), black hole–neutron star binaries (BHNSs), and binary black holes (BBHs) from redshift zero up to six. The binary merger rate per galaxy strongly correlates with the stellar mass of the host galaxy at any redshift considered here. This correlation is significantly steeper for BNSs than for both BHNSs and BBHs. Moreover, we find that the merger rate per galaxy depends also on host galaxy's star formation rate (SFR) and metallicity. We derive a robust fitting formula that relates the merger rate per galaxy with galaxy's SFR, stellar mass, and metallicity at different redshifts. The typical masses of the host galaxies increase significantly as redshift decreases, as a consequence of the interplay between delay time distribution of compact binaries and cosmic assembly of galaxies. Finally, we study the evolution of the merger rate density with redshift. At low redshift ($z \leq 0.1$) early-type galaxies give a larger contribution to the merger rate density than late-type galaxies. This trend reverts at $z \geq 1$.

Key words: black hole physics – gravitational waves – methods: numerical – stars: mass-loss – galaxies: stellar content.

1 INTRODUCTION

The first and second observing runs (O1 and O2) of the LIGO-Virgo collaboration (LVC) led to the detection of 10 binary black holes (BBHs) and one binary neutron star (BNS, Abbott et al. 2016a,d,c, 2017a,c,b, 2018b, 2019), marking the dawn of gravitational-wave (GW) astronomy.

The third observing run (O3) started in 2019 April, and several new GW candidate triggers have already been released. By the end of O3, we expect to have a remarkable population of several tens of BBHs, several new BNSs, and possibly the first merging black hole–neutron star binaries (BHNSs).

KAGRA and LIGO–India will join the detector network soon (see e.g. Somiya 2012; Aso et al. 2013; Abbott et al. 2016b, 2018a), while in about one decade from now third-generation ground-based GW detectors (*Einstein Telescope* and Cosmic Explorer) will lead to a dramatic improvement of sensitivity in GW searches and will be able to catch BBH mergers up to redshift $z \geq 10$ (see e.g. Punturo et al. 2010a,b; Sathyaprakash et al. 2012; Kalogera et al. 2019; GWIC-3G-SCT-Consortium 2019).

A population of several hundred merging compact objects would be a Rosetta stone to address long-standing open questions in astrophysics (Stevenson, Ohme & Fairhurst 2015; Zevin et al. 2017; Fishbach, Holz & Farr 2017; Fishbach, Holz & Farr 2018; Wysocki et al. 2018; Bouffanais et al. 2019): it can provide a key to understand the evolution of massive binary stars (Bethe & Brown 1998; Belczynski, Kalogera & Bulik 2002; Dominik et al. 2013; Mennekens & Vanbeveren 2014; Spera, Mapelli & Bressan 2015; Belczynski et al. 2016; Marchant et al. 2016; Mandel & de Mink 2016; Eldridge & Stanway 2016; Stevenson et al. 2017; Chruslinska et al. 2018; Kruckow et al. 2018; Spera et al. 2019; Mapelli et al. 2019; Eldridge, Stanway & Tang 2019; Giacobbo & Mapelli 2018, 2019), the formation channels of compact binaries (Portegies Zwart & McMillan 2000; Downing et al. 2010; Rodriguez et al. 2015, 2018; Askar et al. 2017; Samsing 2018; Samsing, Askar & Giersz

★ E-mail: Maria.Artale@uibk.ac.at, mcartale@gmail.com

2018; Fragione & Kocsis 2018; Gerosa & Berti 2017; Antonini & Rasio 2016; Banerjee, Baumgardt & Kroupa 2010; Mapelli et al. 2013; Ziosi et al. 2014; Mapelli 2016; Banerjee 2017, 2018; Di Carlo et al. 2019; Bouffanais et al. 2019), and the role of primordial black holes as dark matter candidates (Carr & Hawking 1974; Carr, Kühnel & Sandstad 2016; Bird et al. 2016; Sasaki et al. 2016; Clesse & García-Bellido 2017). Moreover, compact binary mergers can serve as standard sirens to estimate the Hubble constant (Schutz 1986; Abbott et al. 2017d; Chen, Fishbach & Holz 2018; Vitale & Chen 2018; Fishbach et al. 2019; Soares-Santos et al. 2019; The LIGO Scientific Collaboration, the Virgo Collaboration et al. 2019).

Identifying the host galaxies of GW sources is crucial, in order to better understand the astrophysical implications of these events. For example, host galaxy identification is pivotal to measure the Hubble constant (Fishbach et al. 2019; Gray et al. 2019) and gives important clues to reconstruct the formation channels of compact binaries (e.g. star clusters or field). So far, the host galaxy (NGC 4993) was identified only for the BNS merger GW170817 (Abbott et al. 2017e; Abbott et al. 2017f; Goldstein et al. 2017; Savchenko et al. 2017; Margutti et al. 2017; Coulter et al. 2017; Soares-Santos et al. 2017; Chornock et al. 2017; Cowperthwaite et al. 2017; Nicholl et al. 2017; Pian et al. 2017; Alexander et al. 2017).

Theoretical studies can give important contributions on the nature of host galaxies, eventually providing criteria to inform observational campaigns (see e.g. O'Shaughnessy, Kalogera & Belczynski 2010; Dvorkin et al. 2016; Lamberts et al. 2016; Schneider et al. 2017; Cao, Lu & Zhao 2018; Mapelli et al. 2018; Mapelli & Giacobbo 2018; Artale et al. 2019; Marassi et al. 2019; Boco et al. 2019; Conselice et al. 2019; Mapelli et al. 2019). Previous work suggests that the merger rate of compact objects per galaxy in the local Universe strongly correlates with the stellar mass and the star formation rate (SFR) of the host galaxy (e.g. Mapelli et al. 2018; Cao et al. 2018; Artale et al. 2019). Moreover, the typical stellar mass of host galaxies of BNSs might be significantly different from that of merging BBHs and BHNSs, especially at low redshift (Mapelli et al. 2018). This difference comes from the interplay between the distribution of delay times (i.e. the time between the formation of the stellar binary system and the merger event) and the dependence of BBH and BHNS merger efficiency on the metallicity of their progenitor stars (Mapelli et al. 2018; Toffano et al. 2019).

The host galaxies of merging compact objects can be also analysed in terms of early-type (ET) and late-type (LT) galaxies (O'Shaughnessy et al. 2010; Artale et al. 2019), which might help to disentangle the most likely places to detect GW events. Recently, Artale et al. (2019) proposed that ET galaxies host $\gtrsim$60 per cent, $\gtrsim$64 per cent, and $\gtrsim$73 per cent of all the BNSs, BHNSs, and BBHs merging in the local Universe.

In this work, we characterize the host galaxies of merging compact binaries across cosmic time (up to redshift $z \sim 6$), by means of populations synthesis simulations (run with MOBSE, Giacobbo, Mapelli & Spera 2018) combined with galaxy catalogues from the hydrodynamical cosmological simulation EAGLE (Schaye et al. 2015). We show that the merger rate per galaxy strongly correlates with stellar mass, SFR, and metallicity of the host galaxy, and we provide a simple fitting formula. These correlations mildly depend on redshift, tracing the evolution of the host galaxy population.

This paper is organized as follows. Section 2 describes the main properties of EAGLE and MOBSE, and the methodology implemented to seed the EAGLE with a population of merging compact objects (BBHs, BNSs, and BHNSs). We present our results in Section 3. Our main conclusions are discussed in Section 4.

2 METHOD

Following the same methodology originally introduced by Mapelli et al. (2017, see also Mapelli et al. 2018, 2019; Mapelli & Giacobbo 2018; Artale et al. 2019), we combine the results from the population synthesis code MOBSE (Giacobbo et al. 2018) with the galaxy catalogues from the EAGLE simulation (Schaye et al. 2015). In this section, we briefly describe the methodology; further details can be found in the aforementioned papers.

The population synthesis code MOBSE (Giacobbo et al. 2018) built from the BSE code (Hurley, Pols & Tout 2000; Hurley, Tout & Pols 2002) includes new prescriptions for core-collapse supernovae (SNe) based on Fryer et al. (2012), metallicity-dependent stellar winds (see Vink, de Koter & Lamers 2001; Vink & de Koter 2005; Chen et al. 2015), and pair-instability and pulsational pair-instability SNe (Woosley 2017; Spera & Mapelli 2017). Here, we use the catalogue of merging compact objects from the run named CC15α5 from Giacobbo & Mapelli (2018). This run was implemented also in Mapelli et al. (2018), Mapelli et al. (2019), and Artale et al. (2019), because it matches particularly well the local merger rate density of BNSs inferred from GW170817 (Abbott et al. 2019). The main features of CC15α5 are the high efficiency of common envelope ejection ($\alpha = 5$, consistent with recent findings by hydrodynamical simulations of common envelope, Fragos et al. 2019) and the low natal kicks in BNSs (the magnitude of the kick is modelled as a single Maxwellian distribution with 1D root-mean-square velocity $\sigma = 15$ km s^{-1} for both core-collapse SNe and electron-capture SNe). More details about CC15α5 can be found in Giacobbo & Mapelli (2018). In Appendix A, we briefly discuss the impact of our choice of CC15α5 on the main results of this paper. CC15α5 is composed of 12 subsets of metallicities $Z = 0.0002$, 0.0004, 0.0008, 0.0012, 0.0016, 0.002, 0.004, 0.006, 0.008, 0.012, 0.016, and 0.02. Each subset was run with 10^7 stellar binaries, hence the total number of binary systems is 1.2×10^8. For each merging compact binary, the MOBSE catalogue contains information about mass of the primary compact object, mass of the secondary compact object, and delay time.

In this work, we use galaxy catalogues of two runs from the EAGLE suite (Schaye et al. 2015; Crain et al. 2015). The EAGLE simulation, run with a modified version of the code GADGET-3, includes subgrid models to account for star formation, chemical enrichment, radiative cooling and heating, UV/X-ray ionizing background, stellar evolution, asymptotic giant branch stars and SN feedback, and active galactic nucleus (AGN) feedback.

We use the galaxy catalogue from the simulation REFL0100N1504 which represents a periodic box of 100 Mpc side (henceforth we refer to it as EAGLE100) with initially 1504^3 gas and dark matter particles. The initial mass of gas and dark matter particles is $m_{\rm gas} = 1.81 \times 10^6 {\rm M}_\odot$ and $m_{\rm DM} = 9.70 \times 10^6 {\rm M}_\odot$, respectively. In order to test the robustness of our results, we also use the run named RECALL0025N0752RUN, which represents a periodic box of 25 Mpc side (we refer to it as EAGLE25). EAGLE25 was run with the highest resolution in the EAGLE suite; it initially contains 752^3 gas and dark matter particles with $m_{\rm gas} = 2.26 \times 10^5 {\rm M}_\odot$ and $m_{\rm DM} = 1.21 \times 10^6 {\rm M}_\odot$. The two simulated boxes are complementary, since EAGLE25 has the highest resolution in the EAGLE suite (McAlpine et al. 2016), while EAGLE100 contains massive galaxies with stellar masses up to $1.9 \times 10^{12} {\rm M}_\odot$. Hence, by comparing the results of EAGLE25 and

Table 1. Fits of the BNS merger rate per galaxy, from EAGLE100 at $z = 0.1$, 1, 2, and 6 (see Section 3.1 for details).

		BNSs			
		$z = 0.1$	$z = 1$	$z = 2$	$z = 6$
Fit 1D	α_1	1.038 ± 0.001	1.109 ± 0.001	1.050 ± 0.001	1.027 ± 0.003
	α_2	−6.090 ± 0.010	−6.214 ± 0.006	−5.533 ± 0.006	−5.029 ± 0.021
Fit 2D	β_1	0.800 ± 0.002	0.964 ± 0.001	0.977 ± 0.001	1.113 ± 0.003
	β_2	0.323 ± 0.002	0.155 ± 0.001	0.068 ± 0.001	−0.070 ± 0.002
	β_3	−3.555 ± 0.018	−4.819 ± 0.013	−4.874 ± 0.011	−5.764 ± 0.026
Fit 3D	γ_1	0.701 ± 0.002	0.896 ± 0.002	1.018 ± 0.002	1.137 ± 0.004
	γ_2	0.356 ± 0.002	0.184 ± 0.001	0.048 ± 0.001	−0.082 ± 0.002
	γ_3	0.411 ± 0.005	0.222 ± 0.003	−0.103 ± 0.002	−0.053 ± 0.004
	γ_4	−1.968 ± 0.026	−3.795 ± 0.019	−5.451 ± 0.017	−6.104 ± 0.037

EAGLE100 we can estimate the robustness of our findings with respect to resolution and box-size related issues.

In the main text, we discuss the results of EAGLE100 only. We present the results of EAGLE25 and compare them with EAGLE100 in Appendix B. We find very good agreement between the results we obtain with EAGLE100 and those with EAGLE25.

Information on the simulated galaxies is available on the SQL data base.[1] The EAGLE suite adopts the Λ cold dark matter cosmology with parameters inferred from Planck Collaboration et al. (2014) ($\Omega_m = 0.2588$, $\Omega_\Lambda = 0.693$, $\Omega_b = 0.0482$, and $H_0 = 100\,h$ km s^{-1} Mpc^{-1} with $h = 0.6777$). The simulation was run from $z = 127$ up to $z \sim 0$. From the data base, we can extract the properties of the host galaxies (e.g. stellar mass M_*, SFR, and metallicity of star-forming gas).

With a Monte Carlo algorithm, we assign a number of compact binaries (from MOBSE simulations) to each EAGLE stellar particle, based on its initial mass and metallicity. The formation time of compact-binary progenitors assigned to a given EAGLE particle is assumed to be the same as the formation time of the EAGLE particle. Each compact binary merges in the same stellar particle to which it was assigned (we do not allow for ejections of compact binaries) after its individual delay time (estimated from MOBSE). Following this procedure, we assign to each EAGLE galaxy a population of merging compact objects across cosmic time.

In this work, we study the host galaxies of BBHs, BHNSs, and BNSs at four representative redshift intervals: $z = 0$–0.1 (studied also in Artale et al. 2019), $z = 0.93$–1.13, 1.87–2.12, and 5.73–6.51. Hereafter, we will refer to these redshift intervals as $z = 0.1$, 1, 2, and 6 for brevity. The first interval ($z = 0.1$) is our local Universe sample, while $z = 1$ is representative of the advanced LIGO and Virgo horizon for BBHs at design sensitivity. Redshift $z = 2$ corresponds to the peak of star formation, while redshift $z = 6$ is approximately the end of the reionization epoch (we do not consider higher redshifts because the EAGLE suite does not include prescriptions for population III stars).

We select only galaxies with stellar mass above $10^7\,M_\odot$ and SFR $> 0\,M_\odot$ yr^{-1}. Hence, the catalogue from EAGLE100 has in total 77959, 91294, 116074, and 50544 galaxies at $z = 0.1$, 1, 2, and 6, respectively. In the EAGLE25, we get 3070, 1827, 1806, and 412 galaxies at $z = 0.1$, 1, 2, and 6, respectively.

[1] http://icc.dur.ac.uk/Eagle/, http://virgo.dur.ac.uk/data.php.

3 RESULTS

3.1 Merger rate per galaxy

For each redshift interval, we calculate the number of BNSs, BHNSs, and BBHs merging in each simulated galaxy. This number, divided by the considered time-span (1.84, 0.76, 0.41, and 0.14 Gyr for $z = 0.1$, 1, 2, and 6, respectively), gives the merger rate per galaxy at a given redshift (n_{GW}). Artale et al. (2019) already computed this quantity for the local Universe, using the galaxy catalog from EAGLE25. Here, we extend their analysis by considering both higher redshifts ($z = 1$, 2, and 6) and a larger simulated box.

We then performed a series of fits of increasing complexity and dimensionality that we refer to as Fit 1D, Fit 2D, and Fit 3D, with the following prescriptions:

Fit 1D: we fit the merger rate per galaxy as a function of stellar mass (M_*) only, as

$$\log(n_{GW}/\mathrm{Gyr}) = \alpha_1 \log(M_*/M_\odot) + \alpha_2. \quad (1)$$

Fit 2D: we fit the merger rate per galaxy as a function of both M_* and SFR, as

$$\log(n_{GW}/\mathrm{Gyr}) = \beta_1 \log(M_*/M_\odot) + \beta_2 \log(\mathrm{SFR}/M_\odot \mathrm{yr}^{-1}) + \beta_3. \quad (2)$$

Fit 3D: we fit the merger rate per galaxy as a function of M_*, SFR, and metallicity Z, as

$$\log(n_{GW}/\mathrm{Gyr}) = \gamma_1 \log(M_*/M_\odot) + \gamma_2 \log(\mathrm{SFR}/M_\odot \mathrm{yr}^{-1}) + \gamma_3 \log(Z) + \gamma_4. \quad (3)$$

We adopted a standard linear regression approach using least-squares estimation to derive the values of the coefficients and their standard deviations. The results obtained are presented in Tables 1–3 for BNSs, BHNSs, and BBHs, respectively. These fits can help to identify the most likely host galaxies of merging compact objects according to their SFR, stellar mass, and metallicity.

Fig. 1 shows the evolution of the merger rate per galaxy as a function of stellar mass at $z = 0.1$, 1, 2, and 6, for BNS (left-hand column), BHNS (middle column), and BBHs (right-hand column). In all cases, we have a strong visual correlation between n_{GW} and the stellar mass of the host galaxy (in agreement with the correlation found by Artale et al. 2019, at $z \lesssim 0.1$), that is supported by Fit 1D represented by the red line in Fig. 1. This correlation holds with relatively minor changes for all redshifts considered and is steeper for merging BNSs than for BBHs and BHNSs.

Table 2. Same as Table 1, but for BHNSs.

		BHNSs			
		$z = 0.1$	$z = 1$	$z = 2$	$z = 6$
Fit 1D	α_1	0.824 ± 0.001	0.873 ± 0.001	0.913 ± 0.001	0.965 ± 0.002
	α_2	−4.731 ± 0.008	−4.478 ± 0.008	−4.401 ± 0.007	−4.315 ± 0.018
Fit 2D	β_1	0.711 ± 0.002	0.813 ± 0.002	0.871 ± 0.002	0.985 ± 0.003
	β_2	0.150 ± 0.002	0.064 ± 0.002	0.039 ± 0.001	−0.017 ± 0.001
	β_3	−3.536 ± 0.016	−3.900 ± 0.018	−4.019 ± 0.014	−4.490 ± 0.024
Fit 3D	γ_1	0.833 ± 0.002	1.074 ± 0.002	1.084 ± 0.002	0.978 ± 0.003
	γ_2	0.101 ± 0.002	−0.058 ± 0.002	−0.068 ± 0.001	−0.013 ± 0.002
	γ_3	−0.461 ± 0.004	−0.788 ± 0.004	−0.535 ± 0.003	0.016 ± 0.004
	γ_4	−5.434 ± 0.022	−7.733 ± 0.023	−7.055 ± 0.018	−4.386 ± 0.034

Table 3. Same as Table 1, but for BBHs.

		BBHs			
		$z = 0.1$	$z = 1$	$z = 2$	$z = 6$
Fit 1D	α_1	0.807 ± 0.001	0.813 ± 0.001	0.831 ± 0.001	0.933 ± 0.004
	α_2	−4.310 ± 0.006	−3.845 ± 0.008	−3.600 ± 0.008	−4.190 ± 0.026
Fit 2D	β_1	0.812 ± 0.001	0.840 ± 0.002	0.858 ± 0.002	1.053 ± 0.004
	β_2	−0.006 ± 0.001	−0.029 ± 0.002	−0.026 ± 0.001	−0.098 ± 0.002
	β_3	−4.358 ± 0.013	−4.109 ± 0.018	−3.850 ± 0.015	−5.213 ± 0.034
Fit 3D	γ_1	0.921 ± 0.001	1.134 ± 0.002	1.135 ± 0.002	1.131 ± 0.005
	γ_2	−0.051 ± 0.001	−0.172 ± 0.002	−0.167 ± 0.001	−0.137 ± 0.002
	γ_3	−0.404 ± 0.003	−0.839 ± 0.004	−0.681 ± 0.003	−0.171 ± 0.005
	γ_4	−6.049 ± 0.018	−8.338 ± 0.024	−7.758 ± 0.020	−6.321 ± 0.047

In addition, we find that adding the SFR and metallicity in Fit 2D and Fit 3D helped improve the quality of our fit. Quantitatively, we performed a simple model selection by computing the Bayesian Information Criterion (BIC) for all models (Schwarz 1978; Ando 2010), and found that $\mathrm{BIC_{1D}} > \mathrm{BIC_{2D}} > \mathrm{BIC_{3D}}$, indicating that the fit with more parameters is always preferred. It is worth mentioning that this behaviour is expected as the number of points used to do these fits is quite high and the dimensionality of our fits is low.

For host galaxies of merging BBHs and BHNSs at $z = 0.1$, we find that the relation between the merger rate per galaxy and the stellar mass has a slight change in the slope at $\log(M_*/M_\odot) \sim 10.5$ (see Fig. 1) the correlation becomes steeper if $M_* > 10^{10.5}$ $\mathrm{M_\odot}$. This is also seen but less significant at $z = 1$, and 2. The change of slope is also present in BNS hosts, but is weaker and has an opposite trend with respect to BBHs and BHNSs (i.e. the correlation between merger rate per galaxy and M_* becomes shallower if $M_* > 10^{10.5}$ $\mathrm{M_\odot}$).

The slope change is explained by the interplay between the mass–metallicity relation (MZR) and the strong dependence of BBH and BHNS progenitors on metallicity (see e.g. fig. 14 of Giacobbo & Mapelli 2018). Observational and numerical results have shown that the MZR is steep for galaxies with $M_* \sim 10^{8.5} - 10^{10.5}\mathrm{M_\odot}$, with a turnover for $M_* > 10^{10.5}\mathrm{M_\odot}$ (see e.g. Tremonti et al. 2004; Creasey, Theuns & Bower 2015; Chruslinska & Nelemans 2019). This is the result of the role that stellar feedback and AGN feedback have on the chemical evolution of galaxies. The subgrid model adopted in the EAGLE suite accounts for both these feedbacks and shows the turnover in the MZR (Segers et al. 2016).

As a consequence, galaxies with $M_* > 10^{10.5}$ $\mathrm{M_\odot}$ host more metal-poor stars than galaxies with slightly lower mass. Since the merger efficiency of BBHs and BHNSs is higher at low metallicity, the BBH and BHNS merger rate per galaxy is higher if $M_* > 10^{10.5}$ $\mathrm{M_\odot}$. In contrast, the merger efficiency of BNSs is slightly higher at high metallicity ($Z \geq 0.02$) than at intermediate metallicity ($Z \sim 0.002$, see e.g. fig. 14 of Giacobbo & Mapelli 2018); hence, the slope of the correlation between the BNS merger rate per galaxy and M_* is shallower if $M_* > 10^{10.5}$ $\mathrm{M_\odot}$. We quantify the change in the slope and provide more details in Appendix C.

3.2 Merger probability per a given host's stellar mass and SFR

For each redshift interval, we compute the merger probability in a given bin of host's stellar mass and SFR ($M_{*,\mathrm{i}}$, $\mathrm{SFR_j}$), as

$$d^X_{\mathrm{i,j}} = \frac{N^X_{\mathrm{GW\,i,j}}}{N^X_{\mathrm{tot,\,GW}}}, \tag{4}$$

where $N^X_{\mathrm{GW\,i,j}}$ is the sum of all events of kind X (where $X =$ BNSs, BHNSs, or BBHs) occurring in galaxies with mass in the ith bin (between $M_{*,\mathrm{i}} - \Delta M_*/2$ and $M_{*,\mathrm{i}} + \Delta M_*/2$) and SFR in the jth bin (between $\mathrm{SFR_j} - \Delta\mathrm{SFR}/2$ and $\mathrm{SFR_j} + \Delta\mathrm{SFR}/2$) for a given time span. The normalization $N^X_{\mathrm{tot,GW}}$ corresponds to the total number of mergers in all the galaxies of the simulated box, in a given time-span. As a consequence, summing over all the bins yields $\sum_{i,j} d^X_{\mathrm{i,j}} = 1$.

The merger probability accounts for two different facts: (i) the dependence of the number of compact-binary mergers on stellar mass and SFR of the host galaxy; and (ii) the fact that massive galaxies are less numerous than low-mass galaxies, manifested in the galaxy stellar mass function.

We note that the merger probability per a given host stellar mass and SFR can be interpreted as the probability of having a compact-binary merger for a given stellar mass and SFR. We stress that $d^X_{\mathrm{i,j}}$ represents the merger probability in a given bin of SFRs and stellar masses: it must not be confused with the merger rate per galaxy (which is instead indicated as n_{GW} and is discussed in the previous Section 3.1).

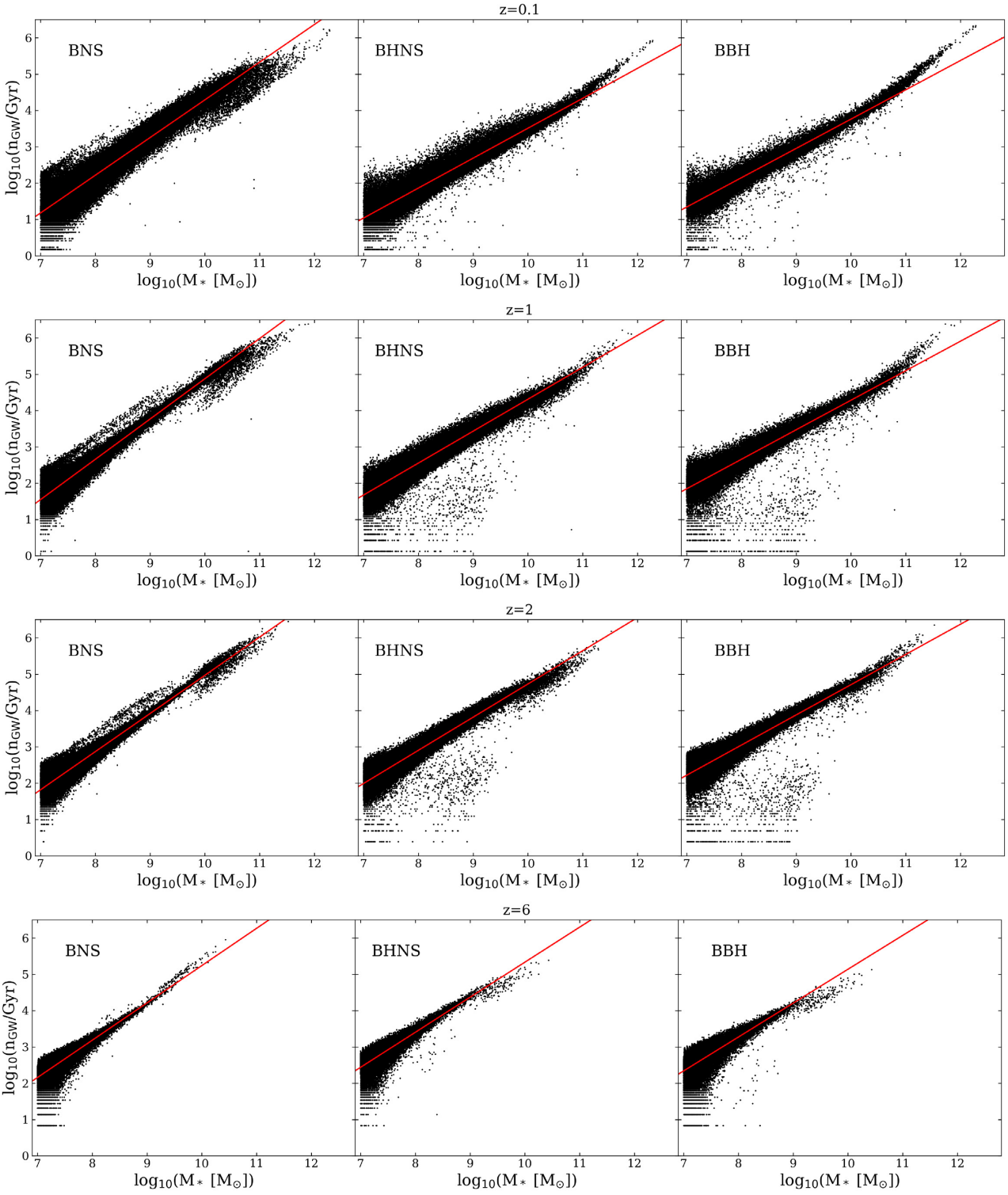

Figure 1. Merger rate per galaxy ($n_{\rm GW}$) as a function of stellar mass M_* for the host galaxies of merging BNSs (left-hand panels), BHNSs (middle panels), and BBHs (right-hand panels), using EAGLE100. From top to bottom row: $z = 0.1$, 1, 2, and 6. Red lines: Fit 1D (see Tables 1–3).

Figs 2, 3 and 4 show the merger probability of BNSs, BBHs, and BHNSs, respectively, as a function of stellar mass and SFR at $z = 0.1$, 1, 2, and 6. In each case, we use a grid of 25 × 25 bins in the range of $\log(M_*/{\rm M}_\odot) \in [7.0, 12.5]$ and $\log({\rm SFR}/{\rm M}_\odot{\rm yr}^{-1}) \in [-5.5, 2.5]$. We find a strong correlation between merger probability, stellar mass, and SFR. This correlation holds for both low and high redshifts. In order to test the robustness of our results, we also computed the merger probability using the galaxy catalog from EAGLE25 finding good agreement between the two simulated boxes. We present the comparison in Appendix B.

Massive galaxies host progressively more compact-binary mergers as redshift decreases. This is apparent from the marginal his-

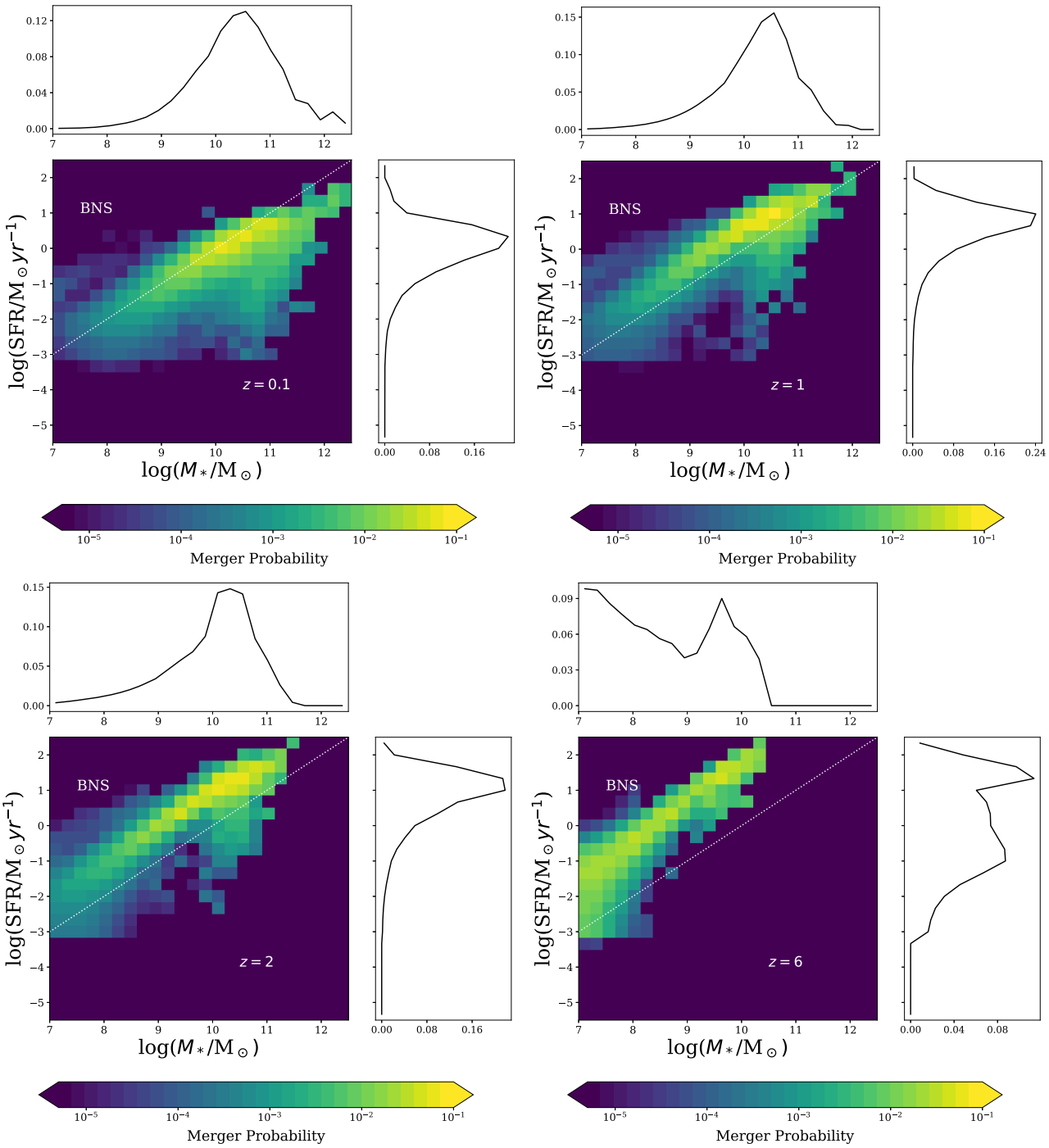

Figure 2. Merger probability per a given SFR and stellar mass (M_*) bin for BNSs, estimated from EAGLE100. The merger probability is calculated as described in equation (4). From top to bottom and from left to right: $z = 0.1$, 1, 2, and 6. The white dotted line represents an sSFR $=10^{-10}$ yr^{-1}. The marginal plots represent the distributions of SFR and M_*.

tograms. To quantify the shift with redshift, we compute the median stellar mass from the marginal probability distributions. For merging BNSs, the median stellar masses of the hosts are $\log(M_*/M_\odot) =$ 10.4, 10.3, 10.2, and 8.4 at $z = 0.1$, 1, 2, and 6, respectively. For merging BHNSs, the median values are $\log(M_*/M_\odot) = 10.7$, 10.2, 9.7, and 8.0, at $z = 0.1$, 1, 2, and 6, respectively. Finally, for merging BBHs, the median stellar masses are $\log(M_*/M_\odot) = 10.9$, 10.3, 9.8, and 7.8 at $z = 0.1$, 1, 2, and 6, respectively. This result is expected since galaxies grow and become more massive with time. The median of the stellar mass distribution for BBH hosts is shifted to a higher mass than for BNS, and BHNS hosts at $z = 0.1$, in agreement with previous works (Cao et al. 2018; Mapelli et al. 2018; Toffano et al. 2019). This trend is reversed at high redshift, where the median is larger for BNS hosts.

Finally, the host galaxy's SFR strongly correlates with M_* at every considered redshift. This is a consequence of the mass–SFR

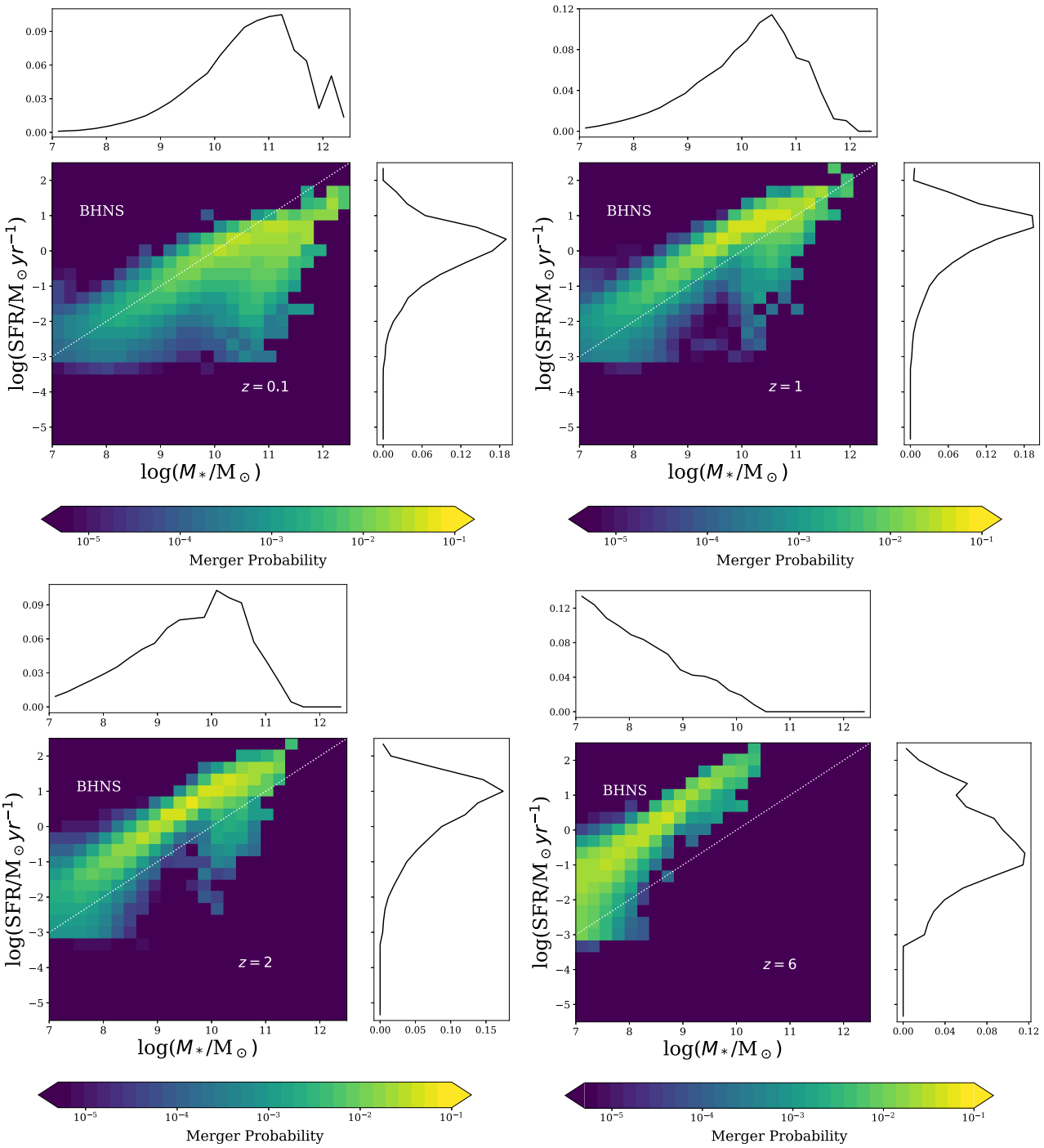

Figure 3. Same as Fig. 2, but for BHNSs.

relation of galaxies (Furlong et al. 2015), as we already discussed in Artale et al. (2019). We also quantify the evolution of SFR with redshift by computing the median SFR of the marginal probability distribution. For merging BNSs, the medians are $\log(\mathrm{SFR}/M_{\odot}\mathrm{yr}^{-1}) = 0.07$, 0.72, 1.0, and 0.02 at $z = 0.1$, 1, 2, and 6, respectively. For merging BHNSs, we get $\log(\mathrm{SFR}/M_{\odot}\mathrm{yr}^{-1}) = 0.09$, 0.65, 0.63, and -0.46 at $z = 0.1$, 1, 2, and 6, respectively. For merging BBHs, we obtain $\log(\mathrm{SFR}/M_{\odot}\mathrm{yr}^{-1}) = 0.12$, 0.65, 0.64, and -0.69 at $z = 0.1$, 1, 2, and 6, respectively. Our results show that the medians of the SFR reflect the evolution of the cosmic SFR in the Universe (Madau & Dickinson 2014), regardless of the kind of merging compact object.

3.3 Merger rate density evolution: early- versus late-type host galaxies

Following Artale et al. (2019), we estimate the contribution to the merger rate density from early-type (R^{ET}) and late-type (R^{LT}) galaxies at $z = 0.1$, 1, 2, and 6. We assume that galaxies with specific star formation rate (sSFR = SFR / M_*) lower

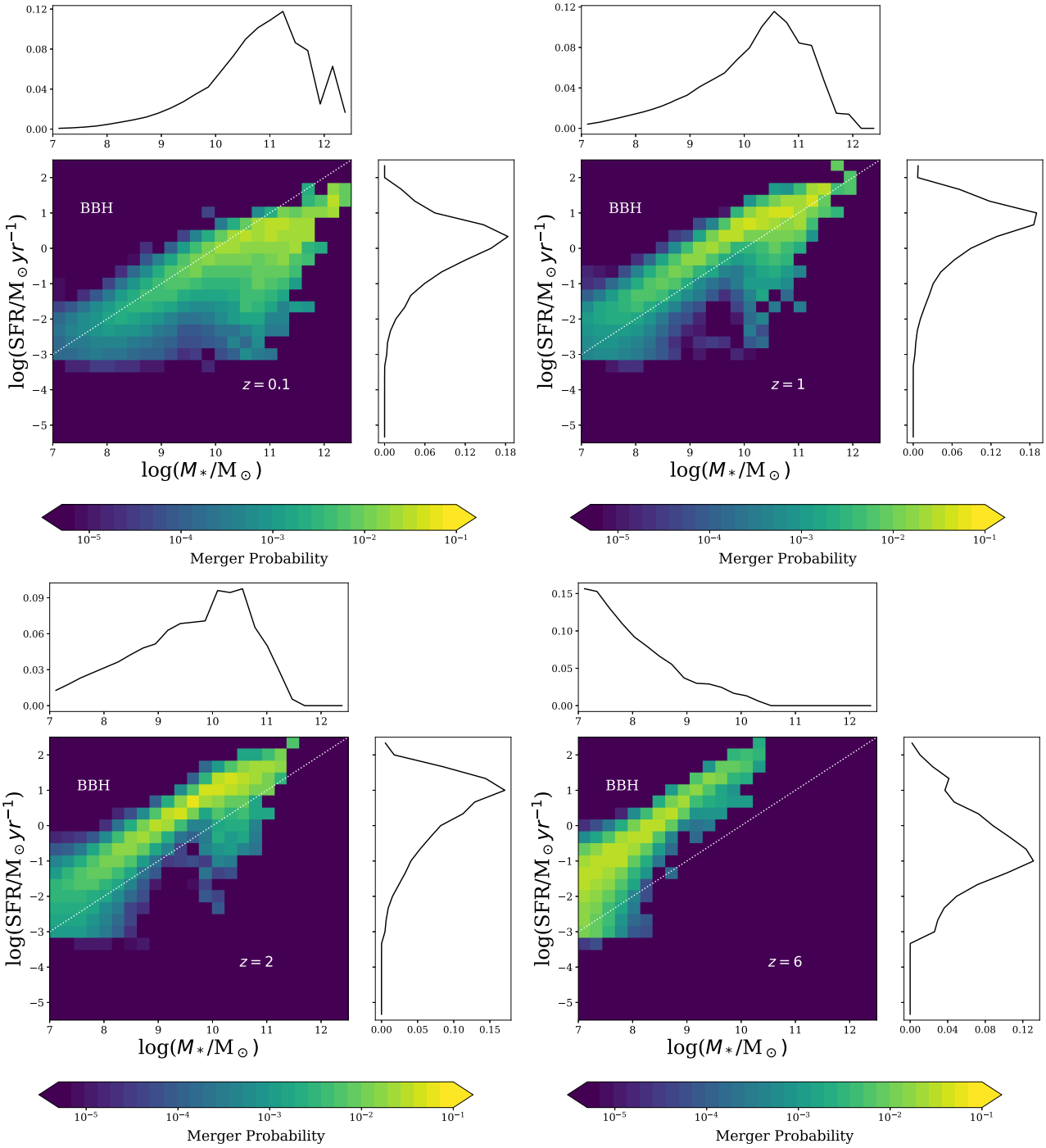

Figure 4. Same as Fig. 2, but for BBHs.

than 10^{-10} yr^{-1} are ET galaxies, while galaxies with sSFR $\geq$ 10^{-10} yr^{-1} are LT galaxies (see white dotted line in Figs 2–4 as reference).

We note that there is no general consensus about the definition of LT and ET galaxies at different redshifts (see e.g. Salim et al. 2007; Karim et al. 2011; Moustakas et al. 2013). Our choice to distinguish between LT and ET galaxies based on an sSFR threshold (sSFR $= 10^{-10}$ yr^{-1}) must be regarded as one of the simplest possible assumption. Different choices do not affect our main results significantly.

Fig. 5 shows the merger rate density of BNSs, BHNSs, and BBHs as a function of redshift. We distinguish between the contribution to the merger rate density from ET galaxies and that from LT galaxies. ET galaxies give a larger contribution to the merger rate density at $z \leq 0.1$ than LT galaxies, in agreement with Artale et al. (2019). The trend reverts at higher redshifts ($z \geq 1$), where most mergers happen in LT galaxies. This result springs from the combination of two effects. On the one hand, ET galaxies become more and more common at low redshift, where they dominate the stellar mass budget (see e.g. Moffett et al. 2016). On the other hand, a

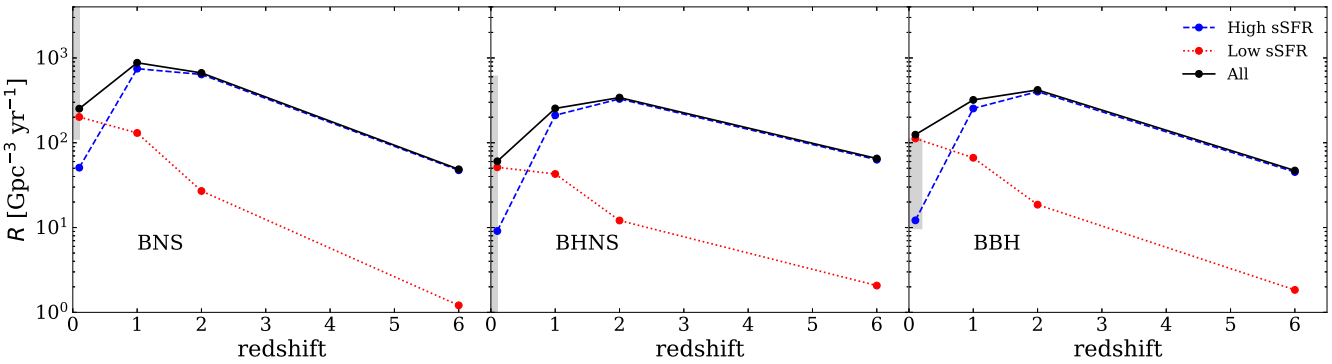

Figure 5. Merger rate density of BNSs (left-hand panel), BHNSs (middle panel), and BBHs (right-hand panel) as a function of redshift. Black circles and solid lines: total merger rate density; red circles and dotted lines: contribution to the merger rate density of ET galaxies; and blue circles and dashed lines: contribution to the merger rate density of LT galaxies. Grey regions: merger rate densities within 90 per cent credible levels reported by the LIGO-Virgo collaboration (Abbott et al. 2018b).

large fraction of compact-binary mergers in the local Universe are characterized by a long delay time (see e.g. Mapelli et al. 2018, 2019): these binary systems were born several Gyr ago in galaxies with high sSFR, but merge at low redshift in galaxies with low sSFR and large stellar mass.

4 CONCLUSIONS

We have characterized the host galaxies of compact-binary mergers across cosmic time, from redshift $z = 0$ to 6, by means of population-synthesis simulations run with the code MOBSE (Mapelli et al. 2017; Giacobbo et al. 2018), combined with galaxy catalogues from the EAGLE cosmological simulations.

We find that there is a strong correlation between the merger rate per galaxy $n_{\rm GW}$ and the stellar mass M_* of the host galaxy. This correlation holds at any redshift considered here. We fit this correlation (Fit 1D) and provide the best-fitting coefficients in Tables 1–3 for BNSs, BHNSs, and BBHs, respectively. The slope of the $n_{\rm GW} - M_*$ correlation is steeper for BNSs than for both BHNSs and BBHs.

Moreover, we showed that including the SFR (Fit 2D) and the combination of SFR–metallicity (Fit 3D) improved the quality of our fit, especially in the latter case. This demonstrates that the merger rate per galaxy depends not only on M_* but also on SFR and Z. Hence, the merger rate per galaxy is maximum in galaxies with high mass, SFR, and metallicity, both at low and high redshifts (although galaxies are smaller at high z and thus the typical mass of the host galaxies decreases with z).

We have shown that our results do not depend significantly on the numerical resolution and on the box size of the cosmological simulation. Indeed, the correlations we find hold for both the EAGLE100 (a 100 Mpc of side comoving box simulation from the EAGLE suite) and the EAGLE25 (a 25 Mpc of side comoving box simulation from the EAGLE suite).

By studying the merger probability as a function of M_* and SFR (Figs 2–4), we find that this quantity evolves significantly with redshift for all considered compact binaries (BNSs, BHNSs, and BBHs). The merger probability accounts for the fact that massive galaxies have a large merger rate per galaxy but are less numerous than low-mass galaxies according to the galaxy stellar mass function.

At low redshift, the merger probability shifts to higher stellar masses and slightly lower SFRs with respect to high redshift. This comes from the interplay between compact-binary delay time and cosmic evolution of the host galaxies. The typical stellar masses of the host galaxies shift to higher values at low redshift, because galaxies grow with time due to cosmic assembly: a large portion of the stellar mass at low redshift is locked into relatively massive galaxies (see e.g. Moffett et al. 2016). Moreover, star formation decreases from $z \sim 2$ to ~ 0. In addition, as only binary compact objects with short delay times are able to merge at high redshift, they tend to merge in the same galaxy where they formed (see e.g. Toffano et al. 2019). In contrast, at low redshift we have both compact binaries that merge with short delay time and compact binaries that formed at high redshift and merge at low redshift with long delay time. Binaries with a long delay time tend to merge in the most massive galaxies, where they ended up after cosmic galaxy assembly (Mapelli et al. 2018).

Finally, we investigated the merger rate density of BNSs, BHNSs, and BBHs (Fig. 5). We distinguish between the contribution to the merger rate density from LT and ET galaxies. At low redshift ($z \leq 0.1$), the contribution to the merger rate from ET galaxies is significantly larger than the one from LT galaxies, while at higher redshift ($z \geq 1$) most mergers occur in LT galaxies. This trend is a consequence of the interplay between cosmic galaxy assembly and the delay time distribution of the compact-object mergers.

Overall, our results predict a strong correlation between the merger rate and the properties (especially stellar mass and SFR) of host galaxies across cosmic time. Ongoing and future searches for electromagnetic counterparts of GW detections will probe this prediction, providing a fundamental test for compact-binary evolution models.

ACKNOWLEDGEMENTS

We acknowledge the anonymous referee and the internal referee of the LVC, Giuseppe Greco, for their careful reading of this paper. MCA acknowledges Darío Rodrigues for useful discussions. MCA and MM acknowledge financial support from the Austrian National Science Foundation through FWF stand-alone grant P31154-N27 'Unraveling merging neutron stars and black hole–neutron star binaries with population synthesis simulations'. MM and YB acknowledge financial support by the European Research Council

for the ERC Consolidator grant DEMOBLACK, under contract no. 770017. MS acknowledges funding from the European Union's Horizon 2020 research and innovation programme under the Marie-Skłodowska–Curie grant agreement no. 794393. MP acknowledges funding from the European Union's Horizon 2020 research and innovation programme under the Marie-Skłodowska–Curie grant agreement no. 664931. We acknowledge the Virgo Consortium for making the EAGLE suite available. The EAGLE simulations were performed using the DiRAC-2 facility at Durham, managed by the ICC, and the PRACE facility Curie based in France at TGCC, CEA, Bruyères-le-Châtel.

REFERENCES

Abbott B. P. et al., 2016a, Phys. Rev.X, 6, 041015
Abbott B. P. et al., 2016b, Living Rev. Relativ., 19, 1
Abbott B. P. et al., 2016c, Phys. Rev. Lett., 116, 061102
Abbott B. P. et al., 2016d, Phys. Rev. Lett., 116, 241103
Abbott B. P. et al., 2017a, Phys. Rev. Lett., 118, 221101
Abbott B. P. et al., 2017b, Phys. Rev. Lett., 119, 141101
Abbott B. P. et al., 2017c, Phys. Rev. Lett., 119, 161101
Abbott B. P. et al., 2017d, Nature, 551, 85
Abbott B. P. et al., 2017e, ApJ, 848, L12
Abbott B. P. et al., 2017f, ApJ, 848, L13
Abbott B. P. et al., 2018a, Living Rev. Relativ., 21, 3
Abbott B. P. et al., 2018b, ApJ, 882, L24
Abbott B. P.et al., 2019, Phys. Rev. X, 9, 031040
Alexander K. D. et al., 2017, ApJ, 848, L21
Ando T., 2010, Bayesian Model Selection and Statistical Modeling. Chapman and Hall/CRC, London
Antonini F., Rasio F. A., 2016, ApJ, 831, 187
Arca Sedda M., Askar A., Giersz M., 2018, MNRAS, 479, 4652
Artale M. C., Mapelli M., Giacobbo N., Sabha N. B., Spera M., Santoliquido F., Bressan A., 2019, MNRAS, 487, 1675
Askar A., Szkudlarek M., Gondek-Rosińska D., Giersz M., Bulik T., 2017, MNRAS, 464, L36
Aso Y., Michimura Y., Somiya K., Ando M., Miyakawa O., Sekiguchi T., Tatsumi D., Yamamoto H., 2013, Phys. Rev. D, 88, 043007
Banerjee S., 2017, MNRAS, 467, 524
Banerjee S., 2018, MNRAS, 473, 909
Banerjee S., Baumgardt H., Kroupa P., 2010, MNRAS, 402, 371
Belczynski K., Kalogera V., Bulik T., 2002, ApJ, 572, 407
Belczynski K., Holz D. E., Bulik T., O'Shaughnessy R., 2016, Nature, 534, 512
Bethe H. A., Brown G. E., 1998, ApJ, 506, 780
Bird S., Cholis I., Muñoz J. B., Ali-Haïmoud Y., Kamionkowski M., Kovetz E. D., Raccanelli A., Riess A. G., 2016, Phys. Rev. Lett., 116, 201301
Boco L., Lapi A., Goswami S., Perrotta F., Baccigalupi C., Danese L., 2019, ApJ, 881, 157
Bouffanais Y., Mapelli M., Gerosa D., Di Carlo U. N., Giacobbo N., Berti E., Baibhav V., 2019, preprint (arXiv:1905.11054)
Cao L., Lu Y., Zhao Y., 2018, MNRAS, 474, 4997
Carr B., Kühnel F., Sandstad M., 2016, Phys. Rev. D, 94, 083504
Carr B. J., Hawking S. W., 1974, MNRAS, 168, 399
Chen Y., Bressan A., Girardi L., Marigo P., Kong X., Lanza A., 2015, MNRAS, 452, 1068
Chen H.-Y., Fishbach M., Holz D. E., 2018, Nature, 562, 545
Chornock R. et al., 2017, ApJ, 848, L19
Chruslinska M., Nelemans G., 2019, MNRAS, 488, 5300
Chruslinska M., Belczynski K., Klencki J., Benacquista M., 2018, MNRAS, 474, 2937
Clesse S., García-Bellido J., 2017, Phys. Dark Universe, 15, 142
Conselice C. J., Bhatawdekar R., Palmese A., Hartley W. G., 2019, preprint (arXiv:1907.05361)
Coulter D. A. et al., 2017, Science, 358, 1556
Cowperthwaite P. S. et al., 2017, ApJ, 848, L17
Crain R. A. et al., 2015, MNRAS, 450, 1937
Creasey P., Theuns T., Bower R. G., 2015, MNRAS, 446, 2125
De Rossi M. E., Bower R. G., Font A. S., Schaye J., Theuns T., 2017, MNRAS, 472, 3354
Dominik M., Belczynski K., Fryer C., Holz D. E., Berti E., Bulik T., Mandel I., O'Shaughnessy R., 2013, ApJ, 779, 72
Downing J. M. B., Benacquista M. J., Giersz M., Spurzem R., 2010, MNRAS, 407, 1946
Dvorkin I., Vangioni E., Silk J., Uzan J.-P., Olive K. A., 2016, MNRAS, 461, 3877
Eldridge J. J., Stanway E. R., 2016, MNRAS, 462, 3302
Eldridge J. J., Stanway E. R., Tang P. N., 2019, MNRAS, 482, 870
Fishbach M. et al., 2019, ApJ, 871, L13
Fishbach M., Holz D. E., Farr B., 2017, ApJ, 840, L24
Fishbach M., Holz D. E., Farr W. M., 2018, ApJ, 863, L41
Fragione G., Kocsis B., 2018, Phys. Rev. Lett., 121, 161103
Fragos T., Andrews J. J., Ramirez-Ruiz E., Meynet G., Kalogera V., Taam R. E., Zezas A., 2019, ApJ, 883, L45
Fryer C. L., Belczynski K., Wiktorowicz G., Dominik M., Kalogera V., Holz D. E., 2012, ApJ, 749, 91
Furlong M. et al., 2015, MNRAS, 450, 4486
Gerosa D., Berti E., 2017, Phys. Rev., D95, 124046
Giacobbo N., Mapelli M., 2018, MNRAS, 480, 2011
Giacobbo N., Mapelli M., 2019, MNRAS, 482, 2234
Giacobbo N., Mapelli M., Spera M., 2018, MNRAS, 474, 2959
Goldstein A. et al., 2017, ApJ, 848, L14
Gray R. et al., 2019, preprint (arXiv:1908.06050)
GWIC-3G-SCT-Consortium, 2019, GWIC 3G Subcommittee Reports. Available at: https://gwic.ligo.org/3Gsubcomm/documents.shtml
Hurley J. R., Pols O. R., Tout C. A., 2000, MNRAS, 315, 543
Hurley J. R., Tout C. A., Pols O. R., 2002, MNRAS, 329, 897
Kalogera V. et al., 2019, BAAS, 51, 242
Karim A. et al., 2011, ApJ, 730, 61
Klencki J., Moe M., Gladysz W., Chruslinska M., Holz D. E., Belczynski K., 2018, A&A, 619, A77
Kruckow M. U., Tauris T. M., Langer N., Kramer M., Izzard R. G., 2018, MNRAS, 481, 1908
Kumamoto J., Fujii M. S., Tanikawa A., 2019, MNRAS, 486, 3942
Lamberts A., Garrison-Kimmel S., Clausen D. R., Hopkins P. F., 2016, MNRAS, 463, L31
Madau P., Dickinson M., 2014, ARA&A, 52, 415
Mandel I., de Mink S. E., 2016, MNRAS, 458, 2634
Mapelli M., 2016, MNRAS, 459, 3432
Mapelli M., Giacobbo N., 2018, MNRAS, 479, 4391
Mapelli M., Zampieri L., Ripamonti E., Bressan A., 2013, MNRAS, 429, 2298
Mapelli M., Giacobbo N., Ripamonti E., Spera M., 2017, MNRAS, 472, 2422
Mapelli M., Giacobbo N., Toffano M., Ripamonti E., Bressan A., Spera M., Branchesi M., 2018, MNRAS, 481, 5324
Mapelli M., Giacobbo N., Santoliquido F., Artale M. C., 2019, MNRAS, 487, 2
Marassi S., Graziani L., Ginolfi M., Schneider R., Mapelli M., Spera M., Alparone M., 2019, MNRAS, 484, 3219
Marchant P., Langer N., Podsiadlowski P., Tauris T. M., Moriya T. J., 2016, A&A, 588, A50
Margutti R. et al., 2017, ApJ, 848, L20
McAlpine S. et al., 2016, Astron. Comput., 15, 72
Mennekens N., Vanbeveren D., 2014, A&A, 564, A134
Moffett A. J. et al., 2016, MNRAS, 462, 4336
Moustakas J. et al., 2013, ApJ, 767, 50
Nicholl M. et al., 2017, ApJ, 848, L18
O'Shaughnessy R., Kalogera V., Belczynski K., 2010, ApJ, 716, 615
Pian E. et al., 2017, Nature, 551, 67
Planck Collaboration XVI et al., 2014, A&A, 571, A16
Portegies Zwart S. F., McMillan S. L. W., 2000, ApJ, 528, L17
Punturo M. et al., 2010a, Class. Quantum Gravity, 27, 084007
Punturo M. et al., 2010b, Class. Quantum Gravity, 27, 194002

Rodriguez C. L., Loeb A., 2018, ApJ, 866, L5
Rodriguez C. L., Morscher M., Pattabiraman B., Chatterjee S., Haster C.-J., Rasio F. A., 2015, Phys. Rev. Lett., 115, 051101
Rodriguez C. L., Chatterjee S., Rasio F. A., 2016, Phys. Rev. D, 93, 084029
Rodriguez C. L., Amaro-Seoane P., Chatterjee S., Kremer K., Rasio F. A., Samsing J., Ye C. S., Zevin M., 2018, Phys. Rev. D, 98, 123005
Salim S. et al., 2007, ApJS, 173, 267
Samsing J., 2018, Phys. Rev. D, 97, 103014
Samsing J., Askar A., Giersz M., 2018, ApJ, 855, 124
Sasaki M., Suyama T., Tanaka T., Yokoyama S., 2016, Phys. Rev. Lett., 117, 061101
Sathyaprakash B. et al., 2012, Class. Quantum Gravity, 29, 124013
Savchenko V. et al., 2017, ApJ, 848, L15
Schaye J. et al., 2015, MNRAS, 446, 521
Schneider R., Graziani L., Marassi S., Spera M., Mapelli M., Alparone M., Bennassuti M. d., 2017, MNRAS, 471, L105
Schutz B. F., 1986, Nature, 323, 310
Schwarz G., 1978, Ann. Stat., 6, 461
Segers M. C., Crain R. A., Schaye J., Bower R. G., Furlong M., Schaller M., Theuns T., 2016, MNRAS, 456, 1235
Soares-Santos M. et al., 2017, ApJ, 848, L16
Soares-Santos M. et al., 2019, ApJ, 876, L7
Somiya K., 2012, Class. Quantum Gravity, 29, 124007
Spera M., Mapelli M., 2017, MNRAS, 470, 4739
Spera M., Mapelli M., Bressan A., 2015, MNRAS, 451, 4086
Spera M., Mapelli M., Giacobbo N., Trani A. A., Bressan A., Costa G., 2019, MNRAS, 485, 889
Stevenson S., Ohme F., Fairhurst S., 2015, ApJ, 810, 58
Stevenson S., Vigna-Gómez A., Mandel I., Barrett J. W., Neijssel C. J., Perkins D., de Mink S. E., 2017, Nat. Commun., 8, 14906
The LIGO Scientific Collaboration et al., 2019, preprint (arXiv:1908.06060)
Toffano M., Mapelli M., Giacobbo N., Artale M. C., Ghirlanda G., 2019, MNRAS, 489, 4622
Tremonti C. A. et al., 2004, ApJ, 613, 898
Vink J. S., de Koter A., 2005, A&A, 442, 587
Vink J. S., de Koter A., Lamers H. J. G. L. M., 2001, A&A, 369, 574
Vitale S., Chen H.-Y., 2018, Phys. Rev. Lett., 121, 021303
Woosley S. E., 2017, ApJ, 836, 244
Wysocki D., Gerosa D., O'Shaughnessy R., Belczynski K., Gladysz W., Berti E., Kesden M., Holz D. E., 2018, Phys. Rev. D, 97, 043014
Zevin M., Pankow C., Rodriguez C. L., Sampson L., Chase E., Kalogera V., Rasio F. A., 2017, ApJ, 846, 82
Ziosi B. M., Mapelli M., Branchesi M., Tormen G., 2014, MNRAS, 441, 3703
Di Carlo U. N., Giacobbo N., Mapelli M., Pasquato M., Spera M., Wang L., Haardt F., 2019, MNRAS, 487, 2947

APPENDIX A: IMPACT OF DIFFERENT POPULATION-SYNTHESIS PRESCRIPTIONS

We expect that the main results presented in Section 3.1 (namely, the slope of the correlation between merger rate per galaxy and stellar mass, SFR, and metallicity) and in Section 3.2 (namely, the merger probability per a given host's stellar mass and SFR) are not significantly affected by the choice of run CC15α5 with respect to other runs presented in Giacobbo & Mapelli (2018), because the merger efficiency (i.e. the number of mergers from a coeval stellar population integrated over a Hubble time) shows approximately the same dependence on metallicity in all of these runs, see fig. 14 of Giacobbo & Mapelli (2018). In particular, BNSs are only marginally affected by progenitor's metallicity, while the merger efficiency of BBHs and BHNSs is up to three orders of magnitude higher at low metallicity than at solar metallicity.

Population-synthesis simulations of isolated binaries obtained with other codes (e.g. Klencki et al. 2018; Kruckow et al. 2018; Chruslinska et al. 2018; Spera et al. 2019) also show a similar trend between merger efficiency and metallicity of the progenitors. Hence, we expect that our main results hold for other binary population-synthesis models, provided that they encode a similar dependence of the merger efficiency on metallicity. In contrast, dynamically formed mergers might lead to some different trend. For example, globular cluster formation happens only in the early Universe, hence it involves mostly metal-poor stars (see e.g. Rodriguez, Chatterjee & Rasio 2016; Rodriguez & Loeb 2018; Askar et al. 2017; Arca Sedda, Askar & Giersz 2018). On the other hand, young star clusters and open clusters efficiently form even at high metallicity and several studies (Mapelli 2016; Di Carlo et al. 2019; Kumamoto, Fujii & Tanikawa 2019) suggest that the merger efficiency from these systems is consistent with the merger efficiency from field binaries. In a follow-up study, we will investigate the impact of dynamically formed binaries on to our main results.

Instead, the normalization of the merger rate density (discussed in Section 3.3) does crucially depend on the chosen population-synthesis model. Several studies (e.g. Mapelli et al. 2017; Mapelli & Giacobbo 2018; Chruslinska et al. 2018; Giacobbo & Mapelli 2018) have shown that the merger rate density varies by orders of magnitude if we change, e.g. natal kick prescriptions and common envelope efficiency. This affects mostly the normalization of the merger rate density, while it has a small effect on the overall evolution with redshift (see e.g. fig. 1 of Mapelli et al. 2017).

APPENDIX B: COMPARISON OF EAGLE25 AND EAGLE100

In the main text, we have discussed the results we obtained from EAGLE100, which represents the largest simulated box from the EAGLE suite. To test how robust our results are in terms of resolution and box size, we perform the same analysis using EAGLE25. The EAGLE25 simulation has a smaller box, but with a larger resolution than EAGLE100 (gas particles are $\sim$8 times smaller in EAGLE25).

Figs B1–B3 show the merger probability density for merging BNSs, BHNSs, and BBHs, respectively, as a function of the stellar mass and SFR of the host galaxies. We bin the stellar mass and SFR using the same binning that we used for EAGLE100. We find that the merger rates obtained with EAGLE25 are similar to those derived from EAGLE100. We note however that EAGLE25 does not have massive clusters, due to the size of the simulated box. Tables B1–B3 show the results of the fits proposed in Section 3.1. Our results show that the coefficients of Fit 1D for EAGLE100 and EAGLE25 are in good agreement, with percentage errors smaller than $\sim$ 8 per cent. This again indicates that the stellar mass of host galaxies of merging compact objects is a crucial property to trace their merger rates. For Fits 2D and 3D, we also find agreement between the two galaxy catalogues, with only few cases showing large discrepancies with percentage errors of the coefficients standing above $\sim$ 20 per cent. It is worth mentioning that only the coefficients attached to SFR and metallicity are concerned. This is expected, because SFR and metallicity are more affected by simulation resolution and box size, as they strongly depend on subgrid prescriptions (see e.g. Furlong et al. 2015; De Rossi et al. 2017).

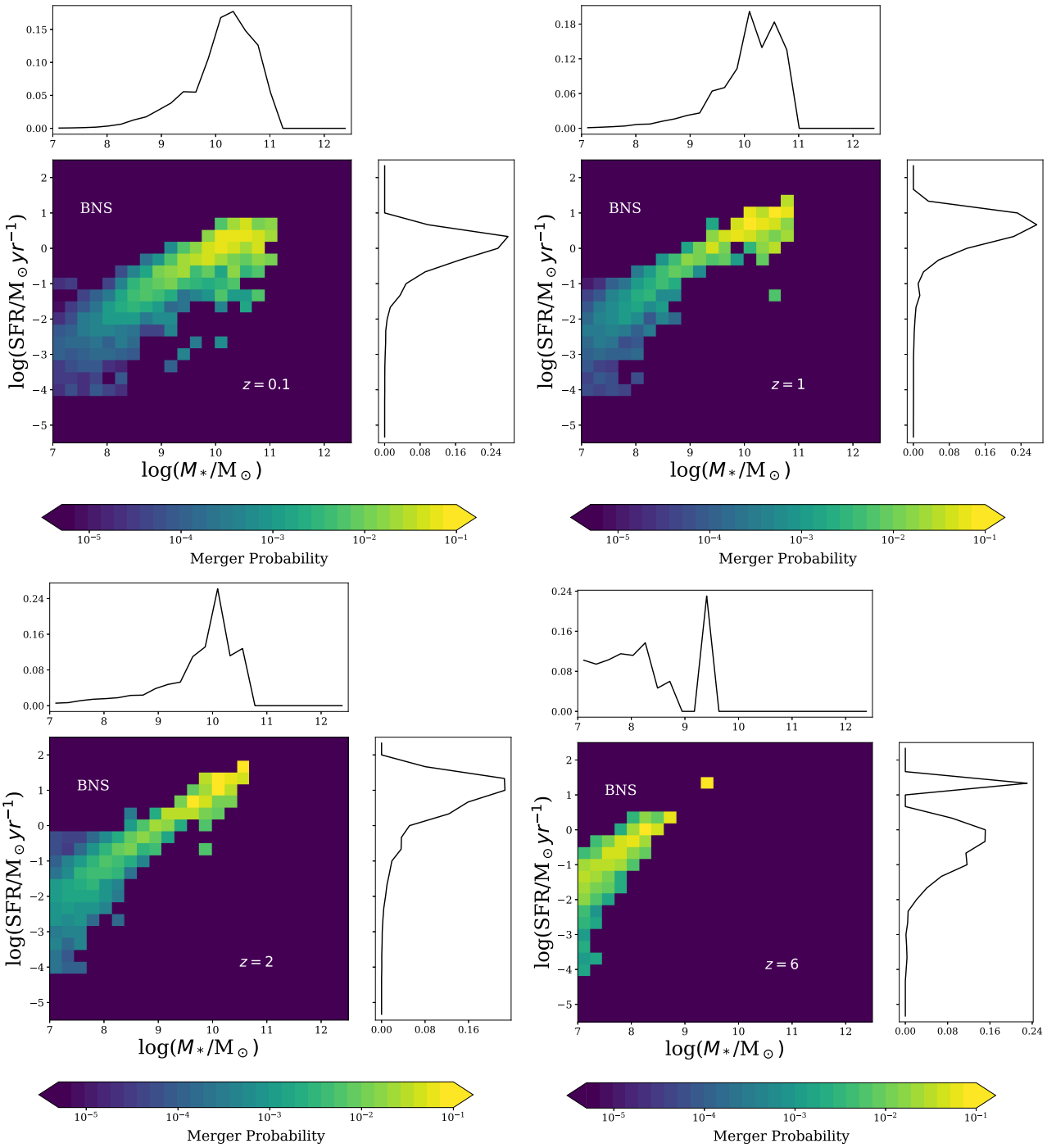

Figure B1. Merger probability for BNSs at redshifts $z = 0.1$, 1, 2, and 6 as a function of the stellar mass and SFR for the EAGLE25 galaxy catalogue. Marginal histograms represent the distributions of SFR and M_*.

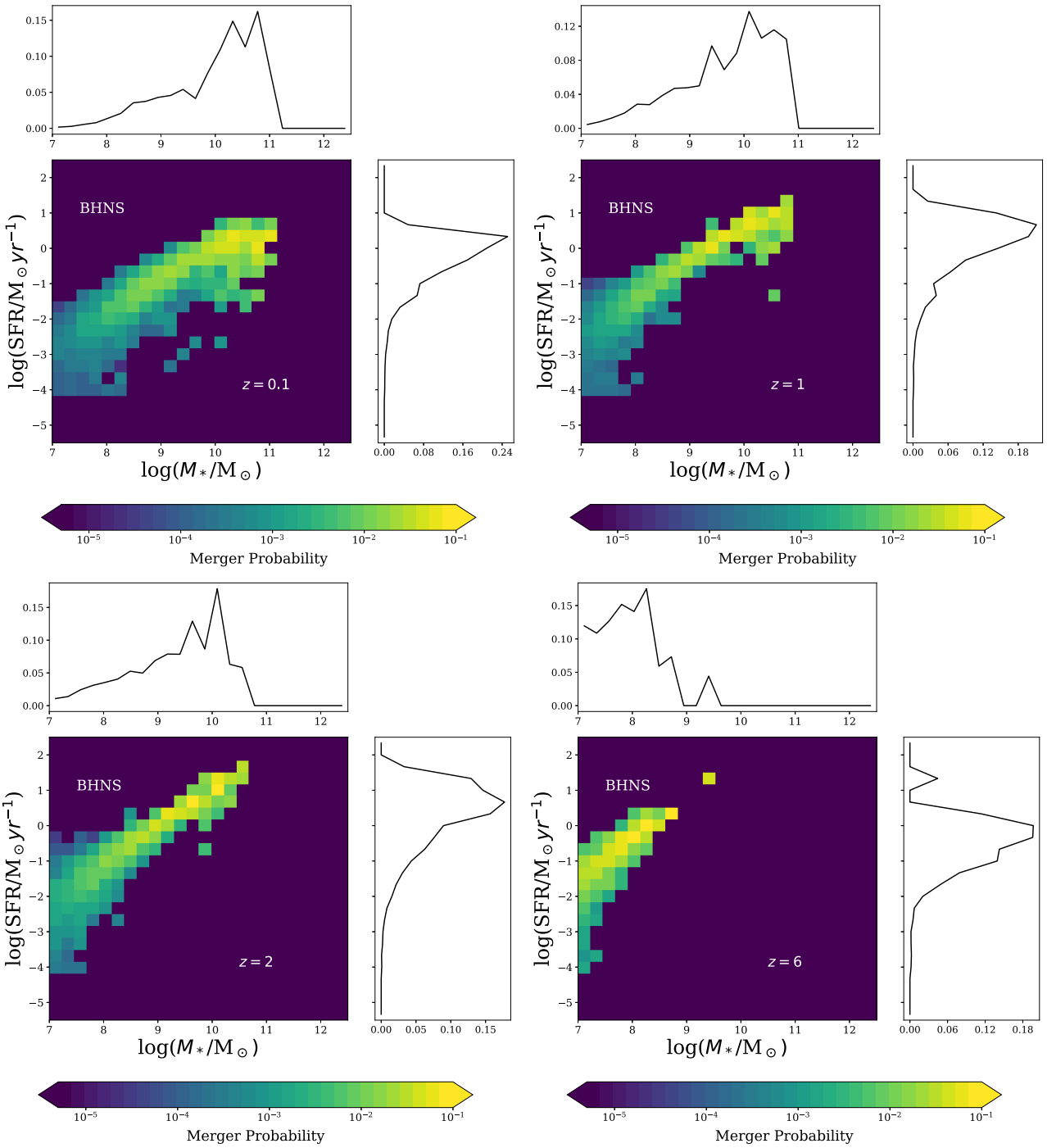

Figure B2. Same as Fig. B1, but for BHNSs.

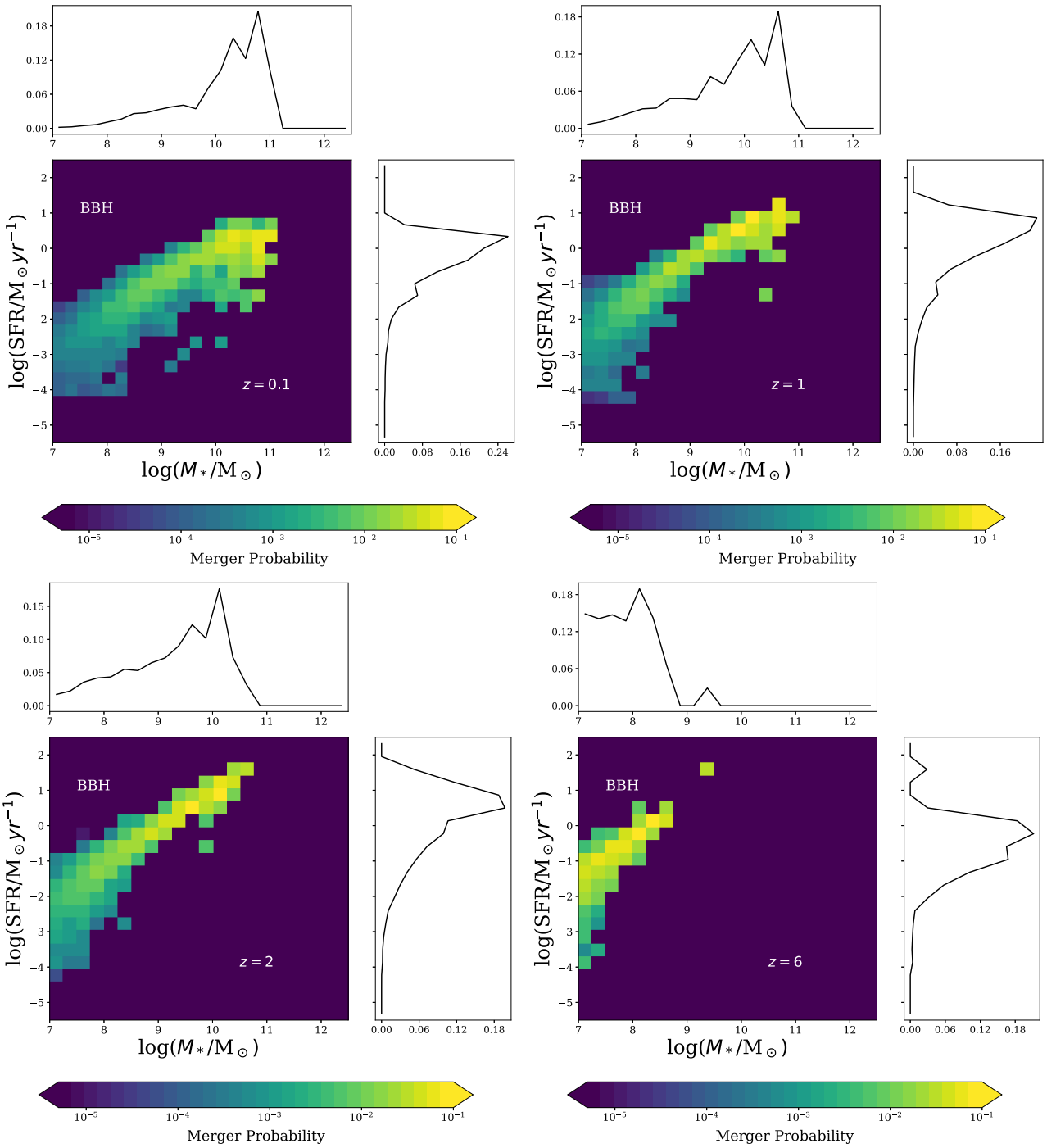

Figure B3. Same as Fig. B1, but for BBHs.

Table B1. Same as Table 1 for BNSs, but using EAGLE25.

		BNSs			
		$z = 0.1$	$z = 1$	$z = 2$	$z = 6$
Fit 1D	α_1	1.073 ± 0.005	1.083 ± 0.005	0.992 ± 0.006	0.999 ± 0.017
	α_2	−6.512 ± 0.046	−6.165 ± 0.039	−5.099 ± 0.044	−4.886 ± 0.130
Fit 2D	β_1	0.865 ± 0.010	1.025 ± 0.010	0.960 ± 0.010	1.021 ± 0.025
	β_2	0.217 ± 0.009	0.053 ± 0.008	0.026 ± 0.007	−0.016 ± 0.013
	β_3	−4.392 ± 0.096	−5.618 ± 0.090	−4.816 ± 0.089	−5.073 ± 0.199
Fit 3D	γ_1	0.852 ± 0.015	1.096 ± 0.015	1.076 ± 0.016	1.054 ± 0.037
	γ_2	0.225 ± 0.011	0.014 ± 0.010	−0.029 ± 0.009	−0.033 ± 0.020
	γ_3	0.031 ± 0.027	−0.136 ± 0.022	−0.235 ± 0.025	−0.067 ± 0.057
	γ_4	−4.214 ± 0.182	−6.553 ± 0.179	−6.386 ± 0.189	−5.524 ± 0.434

Table B2. Same as Table 2 for BHNSs, but using EAGLE25.

		BHNSs			
		$z = 0.1$	$z = 1$	$z = 2$	$z = 6$
Fit 1D	α_1	0.820 ± 0.007	0.850 ± 0.008	0.915 ± 0.006	1.012 ± 0.015
	α_2	−4.510 ± 0.058	−4.149 ± 0.062	−4.357 ± 0.047	−4.726 ± 0.114
Fit 2D	β_1	0.604 ± 0.013	0.719 ± 0.016	0.860 ± 0.011	0.976 ± 0.022
	β_2	0.224 ± 0.012	0.120 ± 0.012	0.046 ± 0.008	0.026 ± 0.011
	β_3	−2.318 ± 0.127	−2.907 ± 0.142	−3.863 ± 0.094	−4.423 ± 0.174
Fit 3D	γ_1	1.011 ± 0.016	1.171 ± 0.020	1.154 ± 0.0143	0.990 ± 0.033
	γ_2	−0.031 ± 0.012	−0.123 ± 0.013	−0.096 ± 0.008	0.019 ± 0.017
	γ_3	−0.994 ± 0.028	−0.874 ± 0.029	−0.598 ± 0.023	−0.029 ± 0.050
	γ_4	−8.036 ± 0.193	−8.863 ± 0.230	−7.862 ± 0.171	−4.619 ± 0.379

Table B3. Same as Table 3 for BBHs, but using EAGLE25.

		BBHs			
		$z = 0.1$	$z = 1$	$z = 2$	$z = 6$
Fit 1D	α_1	0.792 ± 0.006	0.792 ± 0.008	0.838 ± 0.007	0.918 ± 0.019
	α_2	−4.059 ± 0.046	−3.504 ± 0.061	−3.537 ± 0.053	−4.086 ± 0.139
Fit 2D	β_1	0.700 ± 0.011	0.728 ± 0.016	0.850 ± 0.012	0.966 ± 0.027
	β_2	0.095 ± 0.010	0.058 ± 0.013	−0.010 ± 0.009	−0.034 ± 0.014
	β_3	−3.124 ± 0.108	−2.905 ± 0.145	−3.639 ± 0.108	−4.482 ± 0.212
Fit 3D	γ_1	0.993 ± 0.015	1.167 ± 0.020	1.234 ± 0.015	1.096 ± 0.039
	γ_2	−0.090 ± 0.011	−0.176 ± 0.013	−0.196 ± 0.009	−0.104 ± 0.020
	γ_3	−0.699 ± 0.027	−0.851 ± 0.031	−0.782 ± 0.024	−0.269 ± 0.059
	γ_4	−7.211 ± 0.182	−8.684 ± 0.238	−8.867 ± 0.180	−6.305 ± 0.451

APPENDIX C: CHANGE OF SLOPE IN THE MERGER RATE PER GALAXY – M_* CORRELATION

From a visual inspection of Fig. 1, it appears that there is a subtle change of the slope of the $n_{\rm GW} - M_*$ correlation at $\log(M_*/M_\odot) \sim 10.5$ for redshift $z = 0.1$, 1, and 2. This slope change is quite strong for BBHs and BHNSs, while it is barely perceptible for BNSs. Moreover, the slope of the correlation becomes steeper at $\log(M_*/M_\odot) > 10.5$ than at lower galaxy masses in the case of BBHs and BHNSs, while it becomes shallower in the case of BNSs.

We measure how significant the slope change is for the host galaxies of merging BBHs, by comparing the model of Fit 1D from equation (1) with the following model,

$$\log(n_{\rm GW}/{\rm Gyr}) = a\log(M_*/{\rm M}_\odot) + b + c\,\theta(x)\,\log(M_*/{\rm M}_\odot), \quad \text{(C1)}$$

where $\theta(x)$ is the Heaviside step function and $x = \log(M_*/{\rm M}_\odot) - 10.5$. We found that the c coefficient is significant with a p-value of $p < 2 \times 10^{-16}$, corresponding to a value of the t-statistic of 59. We also use the BIC to compare the goodness of the fit for the two models. The BIC can be interpreted as a penalized log-likelihood of the model, where the penalty term takes into account the number of free parameters (Schwarz 1978; Ando 2010). The more negative (or small) the BIC is, the better is the model. For the host galaxies of merging BBHs at $z = 0.1$, we find BIC $=-46089$ for the model without slope change, while BIC $=-49479$ for the model with slope change. We find that the values of R-squared are aligned with our BIC results.

We also compute the BIC for the hosts of BNS and BHNS mergers at $z = 0.1$. In the case of BNSs, we find BIC $=41841$ for the model without slope change, and BIC $=39077$ for the model with slope change. In the case of BHNSs, we find BIC $=-4554$ for the model without slope change, and BIC $=-5162$ for the model with slope change. Our findings indicate that the model with slope change is preferred even in the case of BHNSs and BNSs.

From the linear regression at $\log(M_*/M_\odot) > 10.5$, we get $a = 0.7912 \pm 0.0007$, and $c = 0.504 \pm 0.008$ for BBHs, while $a = 1.063 \pm 0.001$, and $c = -0.81 \pm 0.01$ for BNSs (where a and c are defined in equation C1), confirming the differences in the trend between BBHs and BNSs.

The slope change of the host galaxies of BBH and BHNS mergers arises from the interplay between the MZR of the galaxies and the strong dependence on metallicity of the progenitors. In fact, the MZR is steep for galaxies with $M_* \sim 10^{8.5} - 10^{10.5}\mathrm{M}_\odot$, but has a turnover for masses above $10^{10.5}\mathrm{M}_\odot$ (see e.g. Tremonti et al. 2004; Creasey et al. 2015; Segers et al. 2016). This results from the efficiency of different feedback mechanisms: stellar feedback is the dominant effect in low-mass galaxies, while AGN feedback is the dominant effect for $M_* > 10^{10.5}\mathrm{M}_\odot$.

As a consequence of AGN feedback, galaxies above $10^{10.5}M_\odot$ host stars with a slightly lower metallicity than smaller galaxies, and thus host BBH and BHNS mergers more efficiently. This in turn produces a higher number of merging BBHs and BHNSs in the local Universe, increasing the merger rate per galaxy, n_{GW}.

As shown by Giacobbo et al. (2018), BNS mergers are only marginally affected by the metallicity of the progenitors. Metal-rich progenitors ($Z \sim 0.02$) have slightly higher merger efficiency than intermediate-metallicity ones ($Z \sim 0.002$) in model CC15α5. Hence, the slope break at $10^{10.5}M_\odot$ is present also for BNSs but shows an inverse trend with respect to BBHs and BHNSs (i.e. in the case of BNSs, the slope at $M_* > 10^{10.5}M_\odot$ is shallower than at lower stellar mass).

This paper has been typeset from a TEX/LATEX file prepared by the author.